

# Variational learning of quantum ground states on spiking neuromorphic hardware

Robert Klassert,<sup>1</sup> Andreas Baumbach,<sup>1,2</sup> Mihai A. Petrovici,<sup>2,1</sup> and Martin Gärttner<sup>3,1,4</sup>

<sup>1</sup>*Kirchhoff-Institut für Physik, Ruprecht-Karls-Universität Heidelberg, Im Neuenheimer Feld 227, 69120 Heidelberg, Germany*

<sup>2</sup>*Department of Physiology, University of Bern, 3012 Bern, Switzerland*

<sup>3</sup>*Physikalisches Institut, Universität Heidelberg, Im Neuenheimer Feld 226, 69120 Heidelberg, Germany*

<sup>4</sup>*Institut für Theoretische Physik, Ruprecht-Karls-Universität Heidelberg, Philosophenweg 16, 69120 Heidelberg, Germany*

(Dated: October 5, 2021)

We train a neuromorphic hardware chip to approximate the ground states of quantum spin models by variational energy minimization. Compared to variational artificial neural networks using Markov chain Monte Carlo for sample generation, this approach has the advantage that the neuromorphic device generates samples in a fast and inherently parallel fashion. We develop a training algorithm and apply it to the transverse field Ising model, showing good performance at moderate system sizes ( $N \leq 10$ ). A systematic hyperparameter study shows that scalability to larger system sizes mainly depends on sample quality which is limited by parameter drifts on the analog neuromorphic chip. The learning performance shows a threshold behavior as a function of the number of variational parameters of the ansatz, with approximately 50 hidden neurons being sufficient for representing critical ground states up to  $N = 10$ . The 6+1-bit resolution of the network parameters does not limit the reachable approximation quality in the current setup. Our work provides an important step towards harnessing the capabilities of neuromorphic hardware for tackling the curse of dimensionality in quantum many-body problems.

## I. INTRODUCTION

The Hilbert space of quantum many-body systems and consequently the computational resources required to describe them grow exponentially with system size. On the one hand, this poses a challenge to understanding collective quantum effects, for example in condensed matter physics [1, 2]. On the other hand, efficient numerical tools are required for the characterization and validation of quantum devices such as digital quantum computers currently under development [3]. Fortunately, many physical systems exhibit symmetries and structure that allow to reduce the exponential complexity and to design tractable approaches for the representation of the wave function. For example, so-called stoquastic Hamiltonians are known to have positive ground state wave functions allowing the application of quantum Monte Carlo methods [4]. Locally interacting systems featuring an excitation gap have limited ground state entanglement, which renders tensor network states an efficient method for approximating them [5]. Such physical structure may, however, not always be easy to discover and exploit. As the process of automatically discovering structure despite the curse of dimensionality is a discipline of machine learning, variational approaches using artificial neural networks (ANNs) have found their way into quantum many-body physics in recent years [6]. These so-called *neural quantum states* (NQS) have been shown to serve as efficient function approximators that rival competing approaches like tensor networks in scalability by providing accurate state descriptions using only a small number of parameters. Among other applications NQS have been successfully employed as variational ansätze for ground state search [6–8], quantum dynamics [7, 9–13], and quantum state tomography [14–16].

The most successful existing variational approaches

for representing many-body ground states rely on the use of Markov-chain Monte Carlo (MCMC) methods to generate samples based on which observables are estimated [17]. Probabilistic inference with MCMC in high-dimensional spaces comes with a number of associated challenges such as trading off accuracy against sample correlations and capturing multi-modality within short simulation times. In particular, the sampling of neural network quantum states is known to be a computationally challenging task in the case of restricted Boltzmann machine (RBM) [18]. To tackle this challenge we use a *physical* neuromorphic device which enables the fast generation of independent samples to approximate quantum wave functions.

We develop and demonstrate a method for approximating the ground states of quantum spin systems by variationally adapting the physical parameters of a neuromorphic hardware chip. The neuromorphic chip, depicted in Fig. 1a, functions as a spiking neural network (SNN) emulator. Such networks work in a similar way to neuronal networks in the brain. We use the refractory state of a neuron (refractory,  $z = 1$ , or non-refractory,  $z = 0$ ) to encode the state (up,  $\uparrow$ , or down,  $\downarrow$ ) of a quantum spin (Fig. 1b). SNNs, in contrast to ANNs, have inherent time dynamics and process their inputs in an event-based fashion. Due to the physical implementation the emulation becomes inherently parallel, rendering the sampling speed independent of the network size. We note that neuromorphic hardware has recently been used to represent entangled quantum states using a mapping of general mixed quantum states to a probabilistic representation and training the system to represent a given state by approximating its corresponding probability distribution [19]. Here, instead, we directly encode the wave function of pure quantum states and use this approach for variational ground state search through minimization

of the quantum system's total energy (Fig. 1c,d). Our state representation assumes positive real wave function coefficients, a property which is guaranteed for ground states of stoquastic Hamiltonians [20]. Using the transverse field Ising model (TFIM) as a benchmark case, we find that its ground state can be represented accurately for any value of the transverse field including the quantum phase transition point (Fig. 1e-g).

A systematic hyperparameter study shows that the limiting factors at the current stage are of technical nature and can be overcome by an improved neuromorphic backend. Note that, unlike other functional tasks that SNNs have been employed for in the past [21–23], which only require the reproduction of large scale features, for e.g. image classes, we require the full probability distribution to be sampled with high precision. We therefore demonstrate a new level of sampling precision for neuromorphic systems, which potentially opens up new applications beyond the specific one considered here. Our work thus serves as a demonstration for variational ground state learning on neuromorphic devices. This opens the door to adaptations using alternative, analog or digital neuromorphic hardware [24–26], and the development of improved learning algorithms exploiting fast neuromorphic sample generation.

The remainder of this work is structured as follows: We begin by laying the foundations of spike-based computing (Sec. II A) and the BrainScaleS (BSS) neuromorphic substrate (Sec. II B), followed by details about the variational algorithm, quantum state representation (Sec. II C) and the physical system, namely the TFIM (Sec. II D), which it is applied to. In Sec. III A we examine and discuss the performance of our approach and specifically look at the dependence on system size (Sec. III B), model complexity (Sec. III C), and hardware properties (Sec. III D and Sec. III E). We conclude in Sec. IV and describe future research directions.

## II. BACKGROUND AND METHODS

### A. Spike-based sampling

Generative models based on artificial neural networks can be used to encode and sample from probability distributions [27, 28]. Similarly, spiking neural networks can be shown to approximately implement Markov-chain Monte-Carlo sampling, albeit with dynamics that differ fundamentally from standard statistical methods [29]. Here, we use the BSS neuromorphic platform [30] to encode the wavefunction of quantum spin systems using a two-layer network architecture (Fig. 1c). The implementation is inspired by Boltzmann machines (BM) in that the  $n$  network neurons encode binary values. The *visible* units  $\mathbf{v} = (v_1, \dots, v_N)$  are used to directly represent the quantum spin system and the *hidden* units  $\mathbf{h} = (h_1, \dots, h_{N_h})$  mediate correlations between spins.

We use LIF neurons to implement our network. The

dynamics of such neurons are governed by

$$C_m \frac{du}{dt} = g_l (V_l - u) + I_{\text{syn}}(t), \quad (1)$$

where  $C_m$  is the capacitance of the neuron's membrane,  $u$  its potential,  $V_l$  the leak potential it decays towards via the leak conductance  $g_l$  and  $I_{\text{syn}}$  is the total input current to the neuron. It is formed as a weighted sum over spike-triggered interaction kernels  $\kappa(t)$  for all spikes from all connected neurons. For a detailed discussion we refer to the supplementary materials (SM) [31] and [32].

Whenever the membrane potential  $u$  of a neuron exceeds a threshold value  $V_{\text{thresh}}$ , it generates a spike and the membrane is short-circuited to a reset value  $V_{\text{reset}} < V_{\text{thresh}}$  (Fig. 2b). This reset implements the fixed refractory time  $\tau_{\text{ref}}$  during which we consider the neuron to be in state  $z = 1$  (gray shaded region in Fig. 2b, state  $z = 0$  otherwise). The generated spikes are routed to other neurons via synapses with interaction strength  $w$ .

Under high-frequency Poisson stimulus such networks of LIF neurons can be shown to approximately sample from characteristic Boltzmann distributions [29]. In this scenario, biological neurons enter a high-conductance state with a short membrane time constant  $\tau_m = C_m/g_l \ll \tau_{\text{ref}}$ , and their spike response function is well described by a logistic function

$$p(z = 1|V_l) = \frac{1}{1 + \exp(-[V_l - u_0]/\alpha)}, \quad (2)$$

where  $u_0$  repents the position of and  $\alpha$  the slope at the inflection point. Note that changing  $V_l$  has the same effect as a change of the synaptic input  $I_{\text{syn}}$ . In other words, each neuron effectively calculates  $p(z = 1|I_{\text{syn}})$ , such that the network as a whole can be shown to approximately sample from a Boltzmann distribution  $p_\theta(\mathbf{z}) = \exp[-\epsilon_\theta(\mathbf{z})]$  [29] with network energy  $\epsilon_\theta(\mathbf{z}) = -\sum_{i,j} z_i W_{i,j} z_j / 2 - \sum_i z_i b_i$  and parameters  $\theta = (\mathbf{W}, \mathbf{b})$ .

One can relate the abstract weights  $W_{i,j}$  to the physical strength of the synaptic interaction  $w_{i,j}$  between two neurons and the abstract biases  $b_i$  to the value of the physical leak potential  $V_l$  of each neuron. These two parameter domains are related but have different units. The mapping between physical neuron and synapse parameters and abstract Boltzmann weights can be gauged by measuring the logistic activation function (Eq. 2) with respect to some form of current stimulus (Fig. 2e). This relation neglects some dynamic aspects and as such only holds approximately [29]. This does not restrict the learning scheme applied here. The probability distribution of physical interest is then the marginal over the hidden space

$$p_\theta(\mathbf{v}) = \frac{1}{Z_\theta} \sum_{\mathbf{h}} \exp[-\epsilon_\theta(\mathbf{z})], \quad (3)$$

which is used to encode the ground state wave function (see Sec. II C). The partition sum  $Z_\theta = \sum_{\mathbf{z}} p_\theta(\mathbf{z})$  ensures proper normalization.

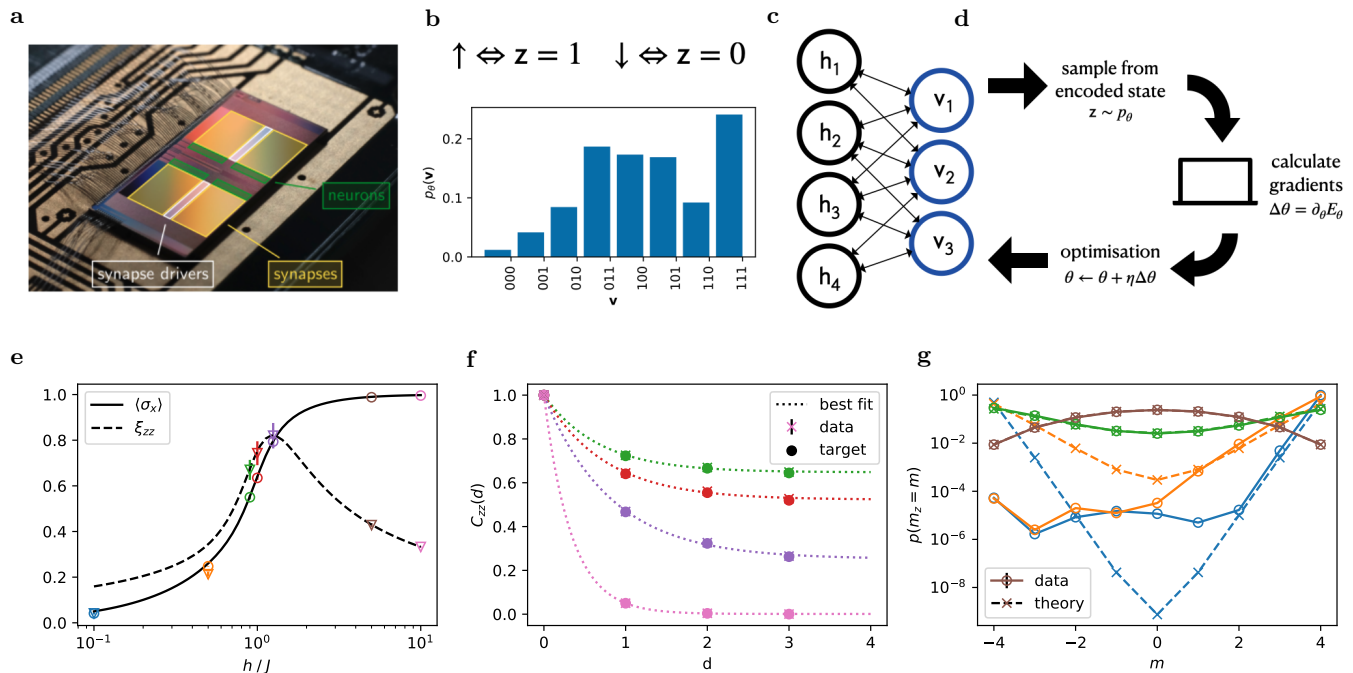


FIG. 1. (a) BrainScaleS-2 neuromorphic chip. This chip implements the accelerated dynamics of up to 512 spiking LIF neurons. (b) Neural network dynamics are interpreted as sampling from a binary probability distribution  $p_\theta(\mathbf{v})$ , where  $z = 1$  is represented by the refractory state of the neuron and  $z = 0$  otherwise. (c) Layered network architecture, where visible states  $\mathbf{v} \in \{0, 1\}^N$  are identified with basis states  $|\mathbf{v}\rangle \in \{|\downarrow\rangle, |\uparrow\rangle\}^{\otimes N}$  of the corresponding quantum spin system. (d) The learning algorithm alternates between on-chip neural sampling and off-chip gradient calculation that informs the network parameter updates  $\Delta\theta$  to minimize the energy of the represented state. (e) Average  $x$ -magnetization  $\langle\sigma_x\rangle$  (circles, solid line) and  $zz$ -correlation length  $\zeta_{zz}$  (triangles, dashed line) for different external fields  $h/J \in \{0.9, 1.0, 1.25, 10.0\}$  [colors as in panel (e)] of an  $N = 8$  spin Ising system. (f)  $zz$ -correlation for different  $h/J \in \{0.1, 0.5, 0.9, 5.0\}$  [colors as in panel (e)] as function of spin distance  $d$ . An exponential fit [Eq. (14), dotted line] was applied to the data (circles) which are in agreement with theory (crosses). (g) Distribution of observed  $z$ -magnetization values for different  $h$ . While for  $h \in \{1, 5\}$  symmetric distributions are learned one observes spontaneous symmetry breaking for the lower field values  $h \in \{0.1, 0.5\}$ .

## B. Neuromorphic chip

We use the BSS physical system, depicted in Fig. 1a, for all experiments reported in this manuscript [30]. BSS is a mixed-signal neuromorphic chip, with 512 adaptive exponential leaky integrate-and-fire (AdEx) neuron circuits, which we configure to implement current-based LIF neurons (see Eq. (1)). Whenever the threshold voltage  $V_{\text{thresh}}$  is surpassed spikes are communicated as digital events and trigger a post-synaptic interaction in downstream neurons.

We employ a routing protocol that forms a freely configurable network of 256 spike sources, combining two neuronal circuits in order to increase the maximum number of sources each neuron can be influenced by to 256. 64 of these we assign to the on-chip (noise) spike generators to provide a pool of stochasticity required for sampling [29]. The full on-chip network structure including both the sampling network and the noise source allocation is shown in Fig. 2c where the bipartite graph shows up in the block structure of the connection matrix (lower part) and the noise sources are randomly assigned from a

fixed pool of 32 excitatory and 32 inhibitory sources (upper part). This leaves us with up to 196 arbitrarily connectable stochastic neurons of which we use a subset to variationally learn the probability distribution representing the ground state wave function of a physical system of interest (see Fig. 1b-d).

For each hardware run the BSS chip returns a list of all (output) spike times and associated neuron IDs. This information combined with the measured  $\tau_{\text{ref}}$  for each neuron is sufficient to reconstruct the network state  $\mathbf{z}(t)$  at any point in time  $t$ . We compute the network state at regular intervals, as visualized in Fig. 2b. The resulting binary configurations are collected in a histogram as shown in Fig. 1b and form an estimate of the steady-state distribution  $p(\mathbf{z})$  of the current network configuration.

## C. Variational algorithm

Our goal is to find an approximation of the ground state of a given *stochastic* Hamiltonian  $H$ . For this we need to determine the parameter set  $\theta$  for which our vari-

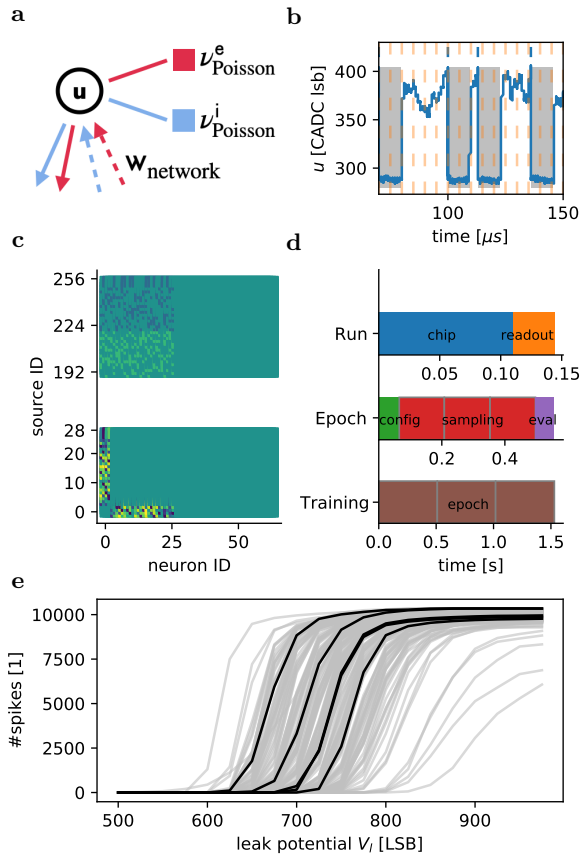


FIG. 2. **(a)** A sampling unit consists of a single LIF neuron under Poisson stimulus (red and blue boxes). Network connectivity is implemented via reciprocal excitatory and inhibitory connections between all neurons (red and blue arrows). **(b)** Exemplary evolution of the membrane potential  $u$ . During the refractory time (shaded area) the neuron is considered to be in state  $z = 1$  and  $z = 0$  otherwise. The state  $z$  is evaluated at regular time intervals (dashed lines). **(c)** Exemplary synaptic weight matrix  $\mathbf{w}$  for  $N = 8$  and  $N_h = 20$ . Unused network parts (inputs 28 to 195 and neurons 64 to 195) are omitted for better visibility. The layered network structure manifests in the block-structure of the lower part. Each neuron is randomly assigned 10 out of the 64 possible noise sources (upper part). **(d)** Distribution of the wall clock time spent during an experimental run. Each epoch starts with a (partial) reconfiguration of the chip (config, green), followed by 3 consecutive sampling runs (red), followed by the evaluation (eval, purple) including the gradient calculation. Each run consists of actual dynamics (blue) and a transfer to the host (orange). **(e)** Neuronal response functions of all 196 neurons. For visibility the first 5 neurons are plotted shown in black.

ational ansatz  $|\psi_\theta\rangle$  of the ground state wave function minimizes the expectation value of the energy:

$$E_\theta = \langle \psi_\theta | H | \psi_\theta \rangle. \quad (4)$$

The restriction to *stochastic* Hamiltonians guarantees that the wave function of the corresponding ground state

has non-negative real coefficients in the chosen basis which is the case if all off-diagonal elements of the Hamiltonian are negative [20]. We use this property to directly identify the probability distribution  $p_\theta(\mathbf{v})$  with the wave function coefficients

$$|\psi_\theta\rangle = \sum_{\mathbf{v}} \sqrt{p_\theta(\mathbf{v})} |\mathbf{v}\rangle, \quad (5)$$

where  $p_\theta(\mathbf{v})$  is estimated by the relative frequency of the occurrence of  $\mathbf{v}$  in the samples generated by the SSN. It resembles the marginal of a Boltzmann distribution [cf. Eq.(3)] as discussed above [29].

We employ a gradient-based minimization of the variational energy  $E_\theta$ . Differentiating Eq. (4) with respect to the parameters  $\theta = (W_{i,j}, b_i)$  results in (see Appendix for details)

$$\partial_{W_{i,j}} E_\theta = \left\langle (E_{\mathbf{v}}^{\text{loc}} - E_\theta) z_i z_j \right\rangle_{p_\theta(\mathbf{z})} \quad (6)$$

$$\partial_{b_k} E_\theta = \left\langle (E_{\mathbf{v}}^{\text{loc}} - E_\theta) z_k \right\rangle_{p_\theta(\mathbf{z})}, \quad (7)$$

where

$$E_{\mathbf{v}}^{\text{loc}} = \sum_{\mathbf{v}'} H_{\mathbf{v}\mathbf{v}'} \sqrt{p_\theta(\mathbf{v}')}/\sqrt{p_\theta(\mathbf{v})} \quad (8)$$

is the local energy. Evaluating the local energies requires access to an estimate of the probabilities  $p_\theta(\mathbf{v}')$  for all states  $\mathbf{v}'$  for which the matrix element  $H_{\mathbf{v}\mathbf{v}'} = \langle \mathbf{v} | H | \mathbf{v}' \rangle$  of the Hamiltonian is non-vanishing. Since no analytical relation between the physical parameters of the spiking network and the abstract parameters  $\theta$  of the RBM is known, we estimate the probabilities  $p_\theta(\mathbf{v})$  from samples. In particular, this means that we need to iterate through the whole collection of generated samples  $\{\mathbf{v}\} \sim p_\theta$  twice. Once to generate the estimate for  $p_\theta(\mathbf{v}')$  and once to calculate  $E_{\mathbf{v}}^{\text{loc}}$ . We implement a gradient descent scheme by alternating between the neuromorphic sampling ( $v, h$ )  $\sim p_\theta$  and host-based gradient calculations (see Fig. 1d). In each iteration the chip is reconfigured according to the gradient given in Eq. 6 and Eq. 7 using the ADAM optimizer (see Appendix). Each training iteration consists of a single hardware (re)configuration followed by multiple sampling runs (see Table 1) of 0.1 s each, which corresponds to  $10^5$  independent samples, and subsequent gradient calculation (see Fig. 2d for relative timings). We emphasize that only the evaluation part scales with the size of the used network and thereby is system-size-independent.

In order to track the accuracy of the algorithm, the true ground states  $|\psi_0\rangle$  and their exact ground state energy  $E_0$  is obtained via exact diagonalization. While reaching small energy deviations

$$\Delta E = \frac{|E - E_0|}{N} \quad (9)$$

indicates that the algorithm has converged to the ground state, we also consider the state overlap with the exact

ground state, i.e. the quantum infidelity

$$1 - F = 1 - |\langle \psi_\theta | \psi_0 \rangle|, \quad (10)$$

to verify the accuracy of the obtained state representation. We train for a large number of iterations (typically 1500) keeping track of energy deviations and infidelities.

#### D. Transverse-field Ising model (TFIM)

We test the above algorithm on the 1D TFIM whose Hamiltonian consists of nearest-neighbor Ising couplings and a homogeneous transverse field,

$$H_{\text{TFIM}} = -J \sum_{\langle i,j \rangle} \sigma_z^i \sigma_z^j - h \sum_{i=1}^N \sigma_x^i, \quad (11)$$

where  $J$  is the interaction strength,  $h$  is the strength of the external field and  $\langle i, j \rangle$  signifies nearest neighbor pairs. Periodic boundary conditions are used such that there is an interaction between spin 1 and spin  $N$ . Furthermore, we consider *ferromagnetic* interactions where  $J > 0$  such that alignment of neighboring spins leads to a lower energy. In this case the Hamiltonian of the TFIM in the  $z$ -basis is stoquastic [20].

In the thermodynamic limit the TFIM features a quantum phase transition at the *critical point*  $J = h$  which separates the ordered phase ( $h < J$ ) where the energy is dominated by the spin-spin interactions  $\sigma_z^i \sigma_z^{i+1}$  from the disordered phase ( $h > J$ ) where spins increasingly align with the  $x$ -axis due to the influence of the external field  $\sigma_x^i$ .

Thus, the two relevant observables are the magnetization in  $x$ -direction

$$\langle \sigma_x \rangle = \frac{\sum_i \langle \sigma_x^i \rangle}{N}, \quad (12)$$

which is also the order parameter of the transition, and the two-point  $zz$ -correlation function

$$C_{zz}(d) = \frac{\sum_i \langle \sigma_z^i \sigma_z^{i+d} \rangle}{N}, \quad (13)$$

where  $d$  is the distance between spins.

Spin-spin correlations generically fall off exponentially,  $C_{zz}(d) \simeq C_0(h) \exp(-d/\xi_{zz}(h))$ , while in the vicinity of the critical point this dependence turns into a power law [33]. Thus the correlation length  $\xi_{zz}$  diverges at the critical point indicating the phase transition point. Since we are dealing with finite systems ( $N \lesssim 10$ ) the phase transition point is shifted and the correlation length stays finite, but becomes maximal there. We also note that in the ferromagnetic phase the ground state is a superposition between two components that are strongly  $z$ -magnetized in either direction, with an energy gap between symmetric and anti-symmetric superposition that

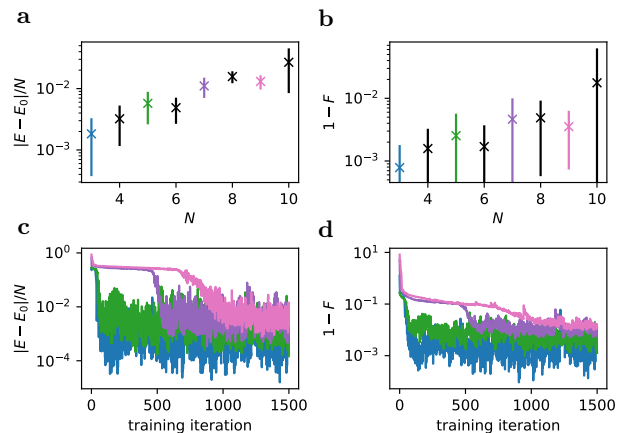


FIG. 3. System-size dependent performance at  $h/J = 1$ . (a),(b) Relative energy mismatch and infidelity between the learned and exact ground state increases at fixed number of hidden units. We report median values and the 15- and 85-percentiles over the last 200 iterations as error bars. (c),(d) Evolution of the approximation quality during learning. For both measures, the time to convergence increases significantly.

vanishes in the limit of  $h/J \rightarrow 0$ . Physically, this leads to spontaneous symmetry breaking in the ferromagnetic phase. Indeed our SNN approximation will also show an analogous symmetry breaking effect.

### III. RESULTS

#### A. Ising phase transition

As described above, we trained a generative model (Fig. 1c,d) using the neuromorphic platform BrainScaleS (Fig. 1a) to represent ground states of the TFIM for a spin chain of size  $N = 8$  at various transversal field strengths  $h$ . The observables shown in Fig. 1e-g have been obtained through sampling from the learned neuromorphic quantum states.

We observe good agreement in the para-magnetic phase while there are deviations in the ferromagnetic regime due to spontaneous symmetry breaking. The learning algorithm has been applied at field strengths  $h \in \{0.1, 0.5, 0.9, 1.0, 1.25, 5, 10\}$ . For each data point slightly different network topologies and sampling parameters were used which are summarized in Table I. Note that these parameters were not optimized and most models are overparameterized and likely oversampled. For  $h = 0.9$  more samples were required in order to learn the symmetric ground state.

The solid line in Fig. 1e is the exact value of  $\langle \sigma_x \rangle$  showing the phase transition from high to low magnetization as the phase transition point is crossed from above. The data points and error bars represent mean values and standard deviations across the final 200 optimization steps of the network-encoded ground states.

TABLE I. Parameter settings for learning the ground state with  $N = 8$  (256 wave function coefficients) at different  $h/J$ .

$h/J$	0.1	0.5	0.9	1.0	1.25	5.0	10.0
$N_{\text{sample}} [10^5]$	2	2	4	2	2	2	2
$N_h$	50	30	40	40	30	20	30
#weights	400	240	320	320	240	160	240
#biases	58	38	48	48	38	28	38

In Fig. 1f the spin-spin correlations in  $z$ -direction  $C_{zz}$  are shown as a function of the spin distance  $d$ . The correlation lengths  $\xi_{zz}$  are extracted by fitting the data points of each field strength with the following function (shown as dotted lines),

$$\hat{C}_{zz}(d) = A \exp(-d/\xi_{zz}) + B \quad (14)$$

where the additional parameters  $A$  and  $B$  account for finite-size effects. The parameters  $\xi_{zz}$  and their standard deviations are shown in Fig. 1e together with the corresponding theoretical values (dashed line). Due to finite size effects we observe that the correlation length has a maximum at  $h/J \approx 1.25$  marking the phase transition point and closely matching the theoretical prediction.

While the points  $h \geq 0.9$  agree well with both observables,  $\langle \sigma_x \rangle$  and  $\xi_{zz}$ , the points at  $h \in \{0.1, 0.5\}$  show significant deviations for the correlation length which, coincidentally, lie on top of the magnetization. In Fig. 1g we show the probabilities for finding the system in a state with  $z$ -magnetization  $m$  (half of the difference between the number of up- and down-spins in  $\mathbf{v}$ ). This reveals that instead of the symmetrical ground state distribution which is learned correctly for  $h \geq 0.9$ , the symmetry is broken for low field values in favor of states with positive  $z$ -magnetization.

Spontaneous symmetry breaking happens here because the wave functions become harder to learn for  $h \rightarrow 0$  as they then increasingly approach a superposition of the two extreme configurations  $|\downarrow\rangle^{\otimes N}$  and  $|\uparrow\rangle^{\otimes N}$ . In terms of SNN dynamics, such a distribution requires both highly synchronous activity and synchronous inactivity. Achieving such a behavior requires distributions with strong local minima, making it hard for any MCMC method to escape. This so-called mixing problem already manifested itself in the increased need for samples at  $h/J = 0.9$  in order to well represent the symmetric ground state. The points below,  $h/J = 0.1, 0.5$  are even further in the ferromagnetic phase which made learning these highly entangled states prohibitively hard with our static stochasticity configuration [34]. We note that the direction of the symmetry breaking can be influenced by an appropriate choice of initial conditions of the network parameters (see Fig. 6 in Appendix).

## B. Dependence on system size

In order to assess the scalability of our approach we study the system-size dependence of the learning perfor-

mance at constant number of network parameters. In the experiment shown in Fig. 3 the number of spins  $N$  is increased from  $N = 3$  to  $N = 10$  for the critical point  $h/J = 1$  while keeping the number of hidden neurons constant (except for  $N = 9$  and 10). Learning is performed with a bipartite network with  $N_h = 40$  and  $N_{\text{sample}} = 2 \cdot 10^5$  samples are drawn in each iteration for  $N = \{3, \dots, 8\}$  and  $N_h = 50$  and  $N_{\text{sample}} = 4 \cdot 10^5$  for  $N \in \{9, 10\}$ . Even though the increased number of hidden neurons and samples for sizes  $N \in \{9, 10\}$  was necessary to ensure convergence of the learning algorithm compared to  $N < 9$  the RBM has less parameters than the number of wave function coefficients ( $509 < 2^9$  and  $560 < 2^{10}$ ).

A quantum fidelity greater than 99% can be achieved and even up to 99.9% for systems  $N < 6$  (Fig. 3b). Since the fidelity imposes a bound on the errors of all possible expectation values good agreement of the learned observables can be expected.

Figures 3c,d show exemplary learning curves of energy error and fidelity as a function of the training iteration. While the learning curves converge quickly for small system sizes, it takes progressively longer to reach good metrics for larger systems, with intermediate regimes of very slow improvement. It should be noted that these plateaus are not observed for  $h/J = 10$ , where the ground state distribution becomes more uniform, which is easy to reach by gradient descent independent of the initial conditions.

We were not able to obtain a good representation of larger system sizes  $N > 10$  at  $h/J = 1$ . The most likely, possibly dependent, causes for this are: (i) diminishing sample quality, (ii) increasing target state complexity (increasing number of wave function coefficients to be learned) hindering convergence. A flawed sampling procedure would cause suboptimal parameter updates and would cause the training to fail to converge (see also the discussion of symmetry breaking at the end of Sec. III A). Larger distributions are expected to require more variational parameters and samples. However, even in the overparameterized and oversampled regime it was not possible to learn ground states for  $N > 10$ . In light of this threshold behaviour a problem with the sampling procedure seems more plausible.

In the following subsections we thoroughly study the impact of substrate induced limitations on the performance of our method: We investigate the dependence of the approximation quality on the size of the parameter space (Sec. III C), the impact of finite weight resolution (Sec. III D) and parameter instabilities of the substrate (Sec. III E).

## C. Dependence on hidden units

In order to assess the required number of hidden units for a good variational representation depending on the system size we have performed a grid search over

$(N, N_h) = (\{3, \dots, 8\}, \{5, 10, 20\})$  drawing  $N_{\text{sample}} = 2 \cdot 10^5$  samples for 1500 training iterations each.

The results are shown in Fig. 4a,b in terms of median energy error per spin and fidelity over the last 200 iterations. While  $N_h = 5$  is sufficient to accurately describe the systems for  $N < 6$ , the fidelity sharply drops to below 90% for larger  $N$  and a respective increase in energy error is observed. Increasing the number of hidden neurons to  $N_h = 10$  we obtain accurate ground state representations up to  $N = 6$  with  $F > 99\%$ , while  $N_h \geq 20$  is required for  $N \in \{7, 8\}$ .

One might expect that more hidden units could decrease the slope of the brown curve ( $N_h = 20$ ) further, also bringing the large systems above 99.9% fidelity. However, comparing with Fig. 3a,b where  $N_h = 40$  was used there is no significant difference in neither energy error nor fidelity, suggesting that model capacity is not the dominating limitation.

Note, that while the system is indeed overparameterized in the sense that there are more variational parameters than wave function coefficients. However, one should keep in mind that the physical network parameters can only be controlled with finite precision. The discreteness of network parameters may limit the representational power of the ansatz as we discuss in the next section.

#### D. Effect of low precision weights

On the BSS system the synaptic weights are implemented by two 6-bit circuits, one for the excitatory and one for the inhibitory part of the synaptic connectome. We use two physical synapses to form a logical synapse which gives an additional bit for the sign. The biases are regulated by adjusting the leak voltage which is controlled by a 10-bit parameter. Due to the circuit design we use less than 9 bits of that. In general these numbers have to be treated as upper bounds due to the analog nature of the system. These design choices are not arbitrary, but reflect various trade-offs between chip resources like the amount of memory that stores these parameters, the inherent variability of analog circuitry and the precision required by applications. Viewed from the application side we are interested in the effect of finite weight resolution on the sampling process.

A lower parameter precision leads to a more coarse grained space of representable distributions. In order to ascertain whether this has a measurable impact, and hence is a limiting factor, we performed an experiment where we randomly initialized RBMs ( $N_v = 8, N_h = 20$ ) with different maximum weight magnitudes  $w_{\text{max}}$  (dynamic range) and compared distributions sampled from the full 7-bit parameters  $p_{7\text{bit}}$  to the distributions obtained by artificially lowering the precision  $p_{\text{disc}}$ . We quantify the distance between these distributions by the Kullback-Leibler divergence (DKL):

$$D_{KL}(p||q) = - \sum_v p(v) \log(p(v)/q(v)). \quad (15)$$

The weights are discretized to equidistant values on the interval  $[-w_{\text{max}}, w_{\text{max}}]$ . For 1-bit only the two interval edges are possible. For  $x$ -bit discretization with  $x > 1$  the grid of possible values spans  $2^x - 1$  states containing 0. Note that all biases were set to the center of the activation functions.

As Fig. 4c shows, we find a quick decrease in DKL as precision grows, which, however, plateaus at 6/7-bit precision. The lack of decrease in DKL from 6-bit to 7-bit is surprising since the number of possible states per weight doubled again. On the other hand, we recognize that at that point we have reached the typical regime of  $\text{DKL} \simeq 10^{-2}$  where the sampling precision saturated for large networks. In view of this, we can conclude that at the maximum weight precision of 7-bit LIF sampling is (just) not limited by parameter precision.

It is worth noting that the number of hidden units was fixed here and no training was performed in order to isolate the effect of low precision weights. Thus, parameter precision might still affect the overall training trajectory or be more important for smaller hidden layers.

#### E. Limitations of the sampling process

A further difference of the BSS chip as compared to digital devices are instabilities and drifts of the analog system parameters. In this section we study the impact of such effects on the sampling and learning performance, by conducting long running sampling experiments of  $T = 10$  s, which is much longer than all other experiments reported in this work. A network for the TFIM ground state search with  $N = 8$  and  $N_h = 20$  was again initialized with an arbitrary weight matrix  $W \sim U[-62, 62]$  and a bias vector corresponding to the inflection points of the activation functions. We performed 10 repetitions of long sampling runs and analyzed the observed samples in three different ways (Fig. 4d). In each case the distribution over samples acquired before time  $t$ ,  $p(t)$ , is calculated and its DKL to a reference distribution is studied as a function of  $t$ :

1. DKL from  $p(t)$  to the distribution of all samples of the run  $p(10\text{s})$  (orange line).
2. DKL from  $p(t)$  to the average distribution over the 10 repetitions  $\langle p(10\text{s}) \rangle$  (blue line).
3. DKL from the distribution  $\tilde{p}(t)$ , obtained after random weight changes, to  $\langle p(10\text{s}) \rangle$  (green line).  $\tilde{p}(t)$  was obtained by randomly changing 15% of the weights by  $\pm 1$  increment (independently for each run) and repeating 10 long sampling runs with the new weights. These random weight changes resembles a learning iteration during the final part of the training where the gradients become close to zero and only randomly flip single parameters.

In each case we show the median result of all sampling runs and the 15th and 85th percentile as errorbars.

The first evaluation measures the convergence to the observed distribution within each run on its own. Here, by construction, convergence is assured and we expect a roughly  $1/N$  behavior of traditional MCMC samplers.

The second evaluation probes the stability of the hardware state between multiple repetitions for a fixed parameter set  $\theta$ . In the above, by calculating weight updates based on samples from multiple short sampling runs, we implicitly assumed that the stability between multiple executions is given. However, Fig. 4d shows that this is not the case and we see a saturation beyond a sampling time of  $t > 0.3$  s.

Finally we change a random subset of all weights by one least-significant-bit (LSB) and measure the change of the distribution caused by this. The flip probability  $p_{\text{flip}} = 0.15$  was chosen such that the resulting DKL is similar to the final observed DKL of the training procedure from Sec. III.A.

The initial decrease indicates that all repetitions are consistently sampling from very similar distributions. The convergence behavior of the first two curves is similar up to 300 ms, showing our choice of 100 ms to be somewhat conservative. Beyond 300 ms only the DKL to the in-trial distribution decreases further (evaluation 1.) and orange line). The divergence of the blue line (from the orange one) beyond 300 ms indicates that even a repetition with the exact same configuration  $\theta$  results in a slightly different distribution  $p_\theta$ . That is, this variation is beyond our configuration control and seems to originate either in temporal variations of the hardware itself or as an artifact of the limited reconfiguration performed between the runs. We suspect that it is the former as the latter is limited to the activation and deactivation of the on-chip noise sources. This behavior creates an implicit upper bound on the accuracy of our trained distributions, as the correctness of the gradients is dependent on the correctness of the sampled distribution. Essentially we apply gradients based on the first repetition onto the configuration of the second – slightly different – distribution, which limits the achievable accuracy of the training scheme. Under these conditions we achieve DKLs of  $1 \times 10^{-3}$  which are slightly better than what we achieve when training against the target distribution ( $7 \times 10^{-3}$ , see Fig. 4c).

Towards the end of the training the gradients and thereby the weight updates become small and most components of the configuration will not change after the finite resolution is taken into account. The number of flips required to achieve a similar DKL is with  $p_{\text{flip}} = 0.15$  nearly an order of magnitude larger than the observed gradient size of 2 – 3%. Naively this would be an indication that the training scheme found a local, rather than a global, minimum. However, our gradient calculation is also distorted by the Boltzmann approximation to the SNN dynamics and we cannot cleanly distinguish which one is the limiting factor.

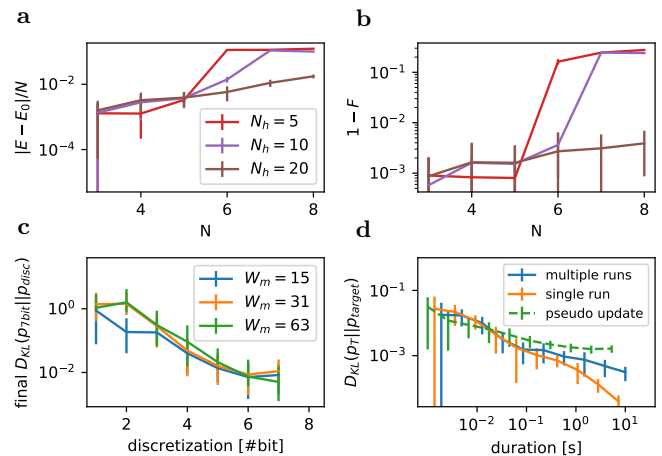


FIG. 4. (a),(b) Dependence of the approximation quality in system size for different sizes of the respective hidden layer of the network, analogous to Fig. 3a,b. Small hidden layers can limit the fidelity of the learned state, especially for larger systems. For the system sizes used here ( $N < 10$ ) hidden layer sizes of  $N_h = 20$  have proven to be sufficient. (c) DKL between the a distribution encoded with maximal weight resolution and artificially coarse grained ones. The resolution only degrades performance after losing two bits. This indicates that the 6+1-bit resolution of BrainScaleS is not limiting for our use case. (d) Sampling quality as a function of hardware execution time. The precision of sampling improves only up to 1 sec for the network architecture  $N = 8$ ;  $N_h = 20$  with an arbitrary set of parameters. Beyond this, trial-to-trial variations (blue) dominate and only the DKL to the in-trial final distribution (orange) decreases further. Both are significantly smaller than a pseudo update which changes 15% of the weights by  $\pm 1$  (green). Note, for visibility reasons we plot alternative times for the different lines.

#### IV. CONCLUSIONS AND OUTLOOK

In summary, we have presented a proof-of-principle of neuromorphic ground state search for quantum spin systems. With our method we have analyzed the TFIM phase transition and found good agreement with theory. We also observed symmetry breaking in the SNN for small transversal fields. The method was found to work for up to  $N = 10$  spins and it was shown that neither the number of hidden units nor the low precision parameters of the analog hardware cause the degradation. The current limitation of the scalability was found to be due to insufficient control over the analog parameters which drift during the sampling process and cause a departure from the encoded quantum state. A second, algorithmic limitation of our learning scheme, arises due to the necessity to obtain all values of  $p_\theta(\mathbf{v})$  from samples, which is expected to require an amount of samples scaling with the number of bins of the distribution, i.e. exponentially in the number of physical spins.

Neither the technical nor the algorithmic challenges are fundamental roadblocks for using neuromorphic hard-



ware for variational learning of quantum states and will be addressed in future research. Advancements in the development of BSS and other neuromorphic hardware platforms [25] will alleviate technical issues as well as introducing new capabilities and tools. Using purely digital neuromorphic chips like for example ODIN [35] or Intel’s Loihi [26], would circumvent the instabilities of an analog system and allow an investigation of the scalability of our models. Thereby, the direct calculation of Boltzmann factors from the weight and bias parameters could become feasible and thus enable the use of learning schemes like in [7] which don’t require a densely sampled visible distribution.

Another promising idea for scalable algorithms is the use of local learning rules that only involve connected neuron pairs since most modern neuromorphic platforms support local on-chip learning. Besides that, it is proven that global gradient-based learning rules like backpropagation for ANNs can be approximated by local learning rules, e.g. by predictive coding [36] or direct feedback alignment [37, 38]. An example for training RBMs with a local learning rule is contrastive divergence [39] of which an event-driven SNN version has been proposed [40]. The question of how to translate these local update schemes to variational ground state learning is left as an important future research direction.

Finally, algorithmic improvements could be enabled by novel encodings of NQS with SNNs. A straightforward idea for encoding not only the amplitudes, but also phases of the wavefunction would be to use additional output units or even a second network like in [14]. Phasor networks represent another avenue for encoding complex numbers with SNNs. It was shown that these networks, which consist of *resonate-and-fire* neurons with complex dynamical variables, can be implemented by integrate-and-fire SNNs and can robustly leverage spike-timing codes [41]. If successful, these approaches to representing complex values in SNNs could enable the extension of the presented variational method to non-stoquastic systems.

## ACKNOWLEDGMENTS

We thank G. Carleo, S. Czischek and T. Gasenzer for discussions. We thank the Electronic Vision(s) group, in particular S. Billaudelle, B. Cramer, J. Schemmel, E. C. Müller, C. Mauch, Y. Stradmann, P. Spilger, J. Weis, and A. Emmel, for maintaining and providing access to the BrainScaleS-2 system and for technical support. This work is supported by the Deutsche Forschungsgemeinschaft (DFG, German Research Foundation) under Germany’s Excellence Strategy EXC 2181/1 – 390900948 (the Heidelberg STRUCTURES Excellence Cluster), by the DFG – project-ID 273811115 – SFB 1225 (ISO-QUANT), by the European Union 7th and Horizon-2020 Framework Programmes, through the ERC Advanced Grant EntangleGen (Project-ID 694561) and under grant agreements 785907, 945539 (HBP), and by the Manfred

Stärk Foundation.

## Appendix A: Derivation of the learning rule

We calculate the derivative of the variational energy with respect to a weight  $W_{ij}$  of the BM assuming a stoquastic Hamiltonian  $H$  and the normalized state representation  $|\psi\rangle = \sum_{\mathbf{v}} \sqrt{p(\mathbf{v})}|\mathbf{v}\rangle$ :

$$\partial_{W_{ij}} E_{\theta} = \partial_{W_{ij}} \sum_{\mathbf{v}\mathbf{v}'} \sqrt{p(\mathbf{v})p(\mathbf{v}')} H_{\mathbf{v}\mathbf{v}'} \quad (\text{A1})$$

$$= \sum_{\mathbf{v}\mathbf{v}'} \sqrt{\frac{p(\mathbf{v}')}{p(\mathbf{v})}} H_{\mathbf{v}\mathbf{v}'} \partial_{W_{ij}} p(\mathbf{v}) \quad (\text{A2})$$

$$= \sum_{\mathbf{v}\mathbf{v}'} \sqrt{\frac{p(\mathbf{v})}{p(\mathbf{v}')}} H_{\mathbf{v}\mathbf{v}'} \cdot \left( \sum_{\mathbf{h}} z_i z_j p(\mathbf{v}') - p(\mathbf{v}) \sum_{\mathbf{z}'} z'_i z'_j p(\mathbf{z}') \right) \quad (\text{A3})$$

$$= \sum_{\mathbf{v}\mathbf{h}} E_i^{\text{loc}} z_i z_j p(\mathbf{z}) - \sum_{\mathbf{i}} E_v^{\text{loc}} p(\mathbf{v}) \sum_{\mathbf{z}'} z'_i z'_j p(\mathbf{z}') \quad (\text{A4})$$

$$= \sum_{\mathbf{z}} (E_v^{\text{loc}} - E_{\theta}) z_i z_j p(\mathbf{z}) \quad (\text{A5})$$

$$= \left\langle (E_v^{\text{loc}} - E_{\theta}) z_i z_j \right\rangle_{p(\mathbf{z})}. \quad (\text{A6})$$

From equation (A2) to (A3) we have used the symmetry of the Hamiltonian. In (A4) the local energy  $E_v^{\text{loc}} = \sum_{\mathbf{v}'} H_{\mathbf{v}\mathbf{v}'} \sqrt{p(\mathbf{v}')}/\sqrt{p(\mathbf{v})}$  is introduced and the variational energy appears in (A5) due to the relation  $E_{\theta} = \sum_{\mathbf{v}} E_v^{\text{loc}} p(\mathbf{v})$ .

To deal with the numerical problem of vanishing entries in  $p_{\theta}(\mathbf{v})$  a small parameter  $\epsilon$  is added to it, essentially introducing a bias towards a uniform distribution. The local energy thus reads  $E_v^{\text{loc}} = \sum_{\mathbf{v}'} H_{\mathbf{v}\mathbf{v}'} \sqrt{p_{\mathbf{v}'} + \epsilon}/\sqrt{p_{\mathbf{v}} + \epsilon}$  where  $\epsilon = 10^{-12}$  was used throughout.

With the above derivation the gradient of the BM,  $\nabla_{\theta} E_{\theta} \equiv \Delta\theta_{\text{BM}}$ , can be estimated as sample average. For the learning scheme we assume that the variational energy gradient with respect to the BSS hardware parameters,  $\Delta\theta_{\text{BSS}}$ , is well approximated by the analogous computation over hardware samples.

## Appendix B: Adaptive momentum optimization

Since the gradient only provides local guidance, it is advisable to scale its components according to the roughness of the cost landscape. An adaptive step size decay probes the cost surface at increasing resolution as the training progresses and bounds the number of steps that need to be computed to reach convergence. We typically employed an exponentially decaying step size

$\alpha(t+1) = \alpha(t) \cdot \gamma_{lr}$  such that  $1/(1 - \gamma_{lr})$  sets a time scale of required optimization steps. We found the values  $\alpha(1) = 1$ ,  $\gamma_{lr} = 0.999$  to work well in practice.

In addition to the fixed step size decay, we employed the Adam scheme [42?] which combines momentum with an adaptive learning rate which is chosen for each network parameter individually. It is a first-order method that estimates mean,  $m(t)$ , and variance,  $v(t)$ , of the gradient by exponential running averages with respective decay rates  $\beta_1$  and  $\beta_2$ :

$$m(t+1) \leftarrow \frac{\beta_1}{1 - \beta_1^t} m(t) + \frac{1 - \beta_1}{1 - \beta_1^t} \Delta\theta_{\text{BSS}}(t) \quad (\text{B1})$$

$$v(t+1) \leftarrow \frac{\beta_2}{1 - \beta_2^t} v(t) + \frac{1 - \beta_2}{1 - \beta_2^t} \Delta\theta_{\text{BSS}}^2(t) \quad (\text{B2})$$

where  $\Delta\theta_{\text{BSS}}^2(t)$  is the component-wise square of the gradient.

The parameters are updated according to the inverted relative error of the gradient where  $m(t)$  acts as a momentum and  $v(t)$  modifies the learning rate

$$\theta_{\text{BSS}}(t+1) \leftarrow \theta_{\text{BSS}}(t) - \eta(t) \frac{m(t)}{\sqrt{v(t)} + \epsilon_{\text{Adam}}}. \quad (\text{B3})$$

The small parameter  $\epsilon_{\text{Adam}}$  is required for regularization purposes. Since  $|\Delta\theta(t)/\sqrt{v(t)}| \leq 1$  the update implicitly adapts the step sizes based on the signal-to-noise ratio of the derivatives. The canonical hyperparameters for Adam are used:  $\beta_1 = 0.9$ ,  $\beta_2 = 0.999$ ,  $\epsilon_{\text{Adam}} = 10^{-8}$ .

### Appendix C: Leaky-integrate-and-fire neurons

The LIF neuron model belongs to the family of continuous spiking neuron models [32]. The neuron's membrane is modeled as a capacitor with capacitance  $C_m$ . It can be charged by the synaptic current stimulus  $I^{\text{syn}}(t)$  while it is constantly discharged across a leak conductance  $g_l$ .

According to Kirchhoff's laws the voltage  $u$  across the capacitance is described by

$$C_m \frac{du(t)}{dt} = g_l(V_l - u(t)) + I^{\text{syn}}(t). \quad (\text{C1})$$

The potential  $V_l$  plays the role of the resting state which is, in the absence of external input, approached on the time scale of the circuit  $\tau_m = C_m/g_l$ .

The spike mechanism is triggered when the membrane potential crosses a threshold  $V_{\text{thresh}}$  from below:

$$u(t_{\text{spike}}) = V_{\text{thresh}} \wedge u'(t_{\text{spike}}) > 0. \quad (\text{C2})$$

After the spike has been fired, the membrane potential is clamped to a reset value during the absolute refractory period  $\tau_{\text{ref}}$ :

$$u(t_{\text{spike}} \leq t \leq t_{\text{spike}} + \tau_{\text{ref}}) = V_{\text{reset}}. \quad (\text{C3})$$

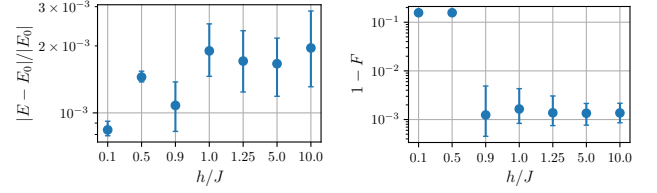


FIG. 5. Relative energy error (left) and infidelity (right) as function of  $h/J$ . Note that the x-axis on the right is not equidistant. The network parameters used in Figs. 5 and 6 are as in Fig. 1.

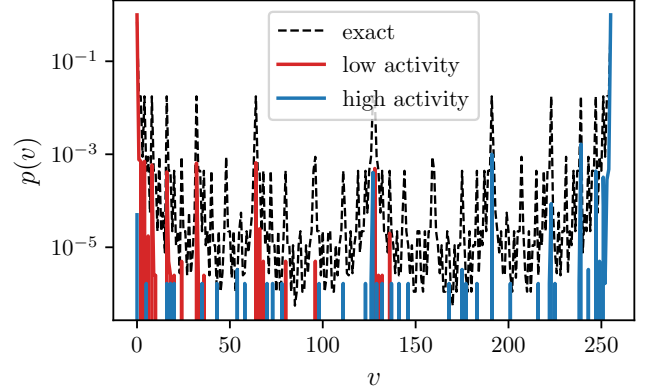


FIG. 6. Symmetry breaking at  $h/J = 0.1$ . Learned probability distribution over visible neuron configurations  $v$  corresponding to basis states of the spin system (solid) compared to the exact ground state distribution (dashed). Standard initialization (blue) favours a high activity state, while an initial negative bias offset on all neurons (red) results in final state with low network activity.

BSS implements current-based synapses in which case synaptic weights carry the unit of current. The spike input of neuron  $j$  is determined by the exponential synaptic kernel  $\kappa(t) = \Theta(t) \exp(-t/\tau_{\text{syn}})$  convolved with spike trains of presynaptic neurons  $S^i(t) = \sum_{t_s} \delta(t - t_s^i)$ :

$$I_j^{\text{syn}}(t) = \sum_i w_{i,j} (S^i \star \kappa)(t) = \sum_i w_{i,j} \sum_{t_s^i} \kappa(t - t_s^i). \quad (\text{C4})$$

The influence of spikes thus decays with the time scale  $\tau_{\text{syn}}$ .

### Appendix D: Supplementary analysis of symmetry breaking

In the experiments shown in Fig. 1 we saw that the symmetry of the ground state was broken for  $h \in \{0.1, 0.5\}$  in favor of "spin up" or simultaneous firing of all visible neurons. This bias for the high activity state might be due to the exponential synaptic kernel's influence extending beyond the refractory period.

Figure 5 shows the energy and infidelity data after training as function of  $h/J$ , respectively. The infidelity with the symmetric ground state suddenly jumps to  $F \approx 10^{-1}$  for the symmetry broken states. The reason why the observables in Fig. 1 were still relatively close to the exact values despite low fidelity is that the energy  $E_\theta = -J \cdot C_{zz}(d=1) - h\langle\sigma_x\rangle$  is minimized. The Hamiltonian is precisely the sum of  $zz$  and  $x$  terms and thus the symmetry broken states at least optimize the sum of

both observables.

By setting an initial negative bias with respect to the neuron's activation functions one can steer the variational algorithm to converge to the opposite symmetry broken state where visible neurons are collectively inhibited. Figure 6 compares the learned state for standard initialization (at the center of the activation functions) and for a shift of  $\Delta b = -2$  LSB with the symmetrical ground state distribution, confirming this effect.

- 
- [1] A. Avella and F. Mancini, eds., *Strongly correlated systems: theoretical methods.*, Springer series in solid-state sciences ed. (Springer-Verlag, Berlin Heidelberg, 2012).
- [2] X. Zhou, W.-S. Lee, M. Imada, N. Trivedi, P. Phillips, H.-Y. Kee, P. Törmä, and M. Eremets, *Nature Reviews Physics* **3**, 462 (2021).
- [3] J. Preskill, *Quantum* **2**, 79 (2018).
- [4] F. Becca and S. Sorella, *Quantum Monte Carlo Approaches for Correlated Systems* (Cambridge University Press, 2017).
- [5] U. Schollwöck, *Ann. Phys.* **326**, 96 (2011).
- [6] J. Carrasquilla, *Advances in Physics: X* **5**, 1797528 (2020).
- [7] G. Carleo and M. Troyer, *Science* **355**, 602 (2017).
- [8] Z.-A. Jia, B. Yi, R. Zhai, Y.-C. Wu, G.-C. Guo, and G.-P. Guo, *Advanced Quantum Technologies* **2**, 1800077 (2019).
- [9] S. Czischek, M. Gärttner, and T. Gasenzer, *Phys. Rev. B* **98**, 024311 (2018).
- [10] M. Schmitt and M. Heyl, *Phys. Rev. Lett.* **125**, 100503 (2020).
- [11] M. J. Hartmann and G. Carleo, *Physical review letters* **122**, 250502 (2019).
- [12] A. Nagy and V. Savona, *Phys. Rev. Lett.* **122**, 250501 (2019).
- [13] M. Reh, M. Schmitt, and M. Gärttner, (2021), arXiv:2104.00013 [cond-mat, physics:physics, physics:quant-ph].
- [14] G. Torlai, G. Mazzola, J. Carrasquilla, M. Troyer, R. Melko, and G. Carleo, *Nature Physics* **14**, 447 (2018).
- [15] J. Carrasquilla, G. Torlai, R. G. Melko, and L. Aolita, *Nat. Mach. Intell.* **1**, 155 (2019).
- [16] G. Torlai and R. G. Melko, *Annual Review of Condensed Matter Physics* **11**, 325 (2020).
- [17] R. G. Melko, G. Carleo, J. Carrasquilla, and J. I. Cirac, *Nature Physics* **15**, 887 (2019).
- [18] P. M. Long and R. A. Servedio, in *Proceedings of the 27th International Conference on International Conference on Machine Learning, ICML'10* (Omnipress, Madison, WI, USA, 2010) p. 703–710.
- [19] S. Czischek, A. Baumbach, S. Billaudelle, B. Cramer, L. Kades, J. M. Pawłowski, M. K. Oberthaler, J. Schemmel, M. A. Petrovici, T. Gasenzer, and M. Gärttner, (2021), arXiv:2008.01039 [cond-mat, physics:quant-ph].
- [20] S. Bravyi, D. P. Divincenzo, R. Oliveira, and B. M. Terhal, *Quantum Information & Computation* **8**, 361 (2008).
- [21] A. F. Kungl, S. Schmitt, J. Klähn, P. Müller, A. Baumbach, D. Dold, A. Kugele, E. Müller, C. Koke, M. Kleider, C. Mauch, O. Breiwieser, L. Leng, N. Gürtler, M. Güttler, D. Husmann, K. Husmann, A. Hartel, V. Karasenko, A. Grübl, J. Schemmel, K. Meier, and M. A. Petrovici, *Front. Neurosci.* **13**, 1201 (2019).
- [22] D. Dold, I. Bytschok, A. F. Kungl, A. Baumbach, O. Breiwieser, W. Senn, J. Schemmel, K. Meier, and M. A. Petrovici, *Neural Networks* **119**, 200 (2019).
- [23] M. A. Petrovici, J. Bill, I. Bytschok, J. Schemmel, and K. Meier, *Phys. Rev. E* **94**, 042312 (2016).
- [24] C. S. Thakur, J. L. Molin, G. Cauwenberghs, G. Indiveri, K. Kumar, N. Qiao, J. Schemmel, R. Wang, E. Chicca, J. Olson Hasler, J. Seo, S. Yu, Y. Cao, A. van Schaik, and R. Etienne-Cummings, *Front. Neurosci.* **12**, 891 (2018).
- [25] K. Roy, A. Jaiswal, and P. Panda, *Nature* **575**, 607 (2019).
- [26] M. Davies, N. Srinivasa, T.-H. Lin, G. China, Y. Cao, S. H. Choday, G. Dimou, P. Joshi, N. Imam, S. Jain, et al., *IEEE Micro* **38**, 82 (2018).
- [27] D. H. Ackley, G. E. Hinton, and T. J. Sejnowski, *Cognitive Science* **9**, 147 (1985).
- [28] G. Hinton, P. Dayan, B. Frey, and R. Neal, *Science* **268**, 1158 (1995).
- [29] M. A. Petrovici, *Form Versus Function: Theory and Models for Neuronal Substrates*, edited by S. I. Publishing (Springer International Publishing, 2016).
- [30] S. Billaudelle, Y. Stradmann, K. Schreiber, B. Cramer, A. Baumbach, D. Dold, J. Göltz, A. F. Kungl, T. C. Wunderlich, A. Hartel, et al., in *2020 IEEE International Symposium on Circuits and Systems (ISCAS)* (IEEE, 2020) pp. 1–5.
- [31] See Supplemental Material at [URL will be inserted by publisher] for details to the learning rule and rate adaptation, as well as further neuron details.
- [32] W. Gerstner, Wulfram, Kistler, and W. M., *Spiking Neuron Models: Single Neurons, Populations, Plasticity* (Cambridge University Press, 2002).
- [33] M. Karl, H. Cakir, J. C. Halimeh, M. K. Oberthaler, M. Kastner, and T. Gasenzer, *Physical Review E* **96**, 022110 (2017).
- [34] A. Korcsak-Gorzo, M. G. Müller, A. Baumbach, L. Leng, O. J. Breiwieser, S. J. van Albada, W. Senn, K. Meier, R. Legenstein, and M. A. Petrovici, arXiv preprint arXiv:2006.11099 (2020).
- [35] C. Frenkel, M. Lefebvre, J.-D. Legat, and D. Bol, *IEEE transactions on biomedical circuits and systems* **13**, 145 (2018).
- [36] J. C. R. Whittington and R. Bogacz, *Neural Computation* **29**, 1229 (2017).
- [37] B. Crafton, A. Parihar, E. Gebhardt, and A. Raychowdhury, *Frontiers in Neuroscience* **13** (2019), 10.3389/fnins.2019.00525.
- [38] J. Lee, R. Zhang, W. Zhang, Y. Liu, and P. Li, *Frontiers*

- in *Neuroscience* **14** (2020), [10.3389/fnins.2020.00143](#).
- [39] G. E. Hinton, in *Neural networks: Tricks of the trade* (Springer, 2012) pp. 599–619.
- [40] E. Neftci, S. Das, B. Pedroni, K. Kreutz-Delgado, and G. Cauwenberghs, *Frontiers in Neuroscience* **7** (2014), [10.3389/fnins.2013.00272](#).
- [41] E. P. Frady and F. T. Sommer, *Proceedings of the National Academy of Sciences* **116**, 18050 (2019).
- [42] D. P. Kingma and J. Ba, [arXiv:1412.6980 \[cs.LG\]](#) (2014).